Assembly of a Concentric Förster Resonance Energy Transfer Relay on a Quantum Dot Scaffold: Characterization and Application to Multiplexed Protease Sensing

W. Russ Algar,[†,⊥,¶,*] Mario G. Ancona,[‡] Anthony P. Malanoski,[†] Kimihiro Susumu,[§,∥] and Igor L. Medintz[†,*]

[†]Center for Bio/Molecular Science and Engineering, Code 6900, [‡]Electronic Science and Technology Division, Code 6876, and [§]Optical Sciences Division, Code 5611, U.S. Naval Research Laboratory, Washington, D.C. 20375, United States, [⊥]College of Science, George Mason University, Fairfax, Virginia 22030, United States, and [∥]Sotera Defense Solutions, Annapolis Junction, Maryland 20701, United States. [¶]Present address: Department of Chemistry, University of British Columbia, Vancouver, BC V6T 1Z1, Canada.

ABSTRACT Semiconductor nanocrystals, or quantum dots (QDs), are one of the most widely utilized nanomaterials for biological applications. Their cumulative physicochemical and optical properties are both unique among nanomaterials and highly advantageous. In particular, Förster resonance energy transfer (FRET) has been widely utilized as a spectroscopic tool with QDs, whether for characterizing QD bioconjugates as a "molecular ruler" or for modulating QD luminescence "on" and "off" in biosensing configurations. Here, we investigate the assembly and utility of a new "concentric" FRET relay that comprises a central QD conjugated with multiple copies of two different peptides, each labeled with one of two fluorescent dyes, Alexa Fluor 555 (A555) or Alexa Fluor 647 (A647). Energy transfer occurs from the QD to the A555 ($FRET_1$) then to the A647 ($FRET_2$) and, to a lesser extent, directly from the QD to the A647 ($FRET_3$). We show that such an arrangement can provide insight into the interfacial distribution of peptides assembled to the QD and can further be utilized for sensing proteolytic activity. In the latter, progress curves for digestion of the assembled peptides by two prototypical proteases, trypsin and chymotrypsin, were measured from the relative QD, A555 and A647 PL contributions, and used to extract Michaelis–Menten kinetic parameters. We further show that the concentric FRET relay, as a single nanoparticle vector, can track the tryptic activation of a proenzyme, chymotrypsinogen, to active chymotrypsin. The concentric FRET relay is thus a potentially powerful tool for the characterization of QD bioconjugates and multiplexed sensing of coupled biological activity.

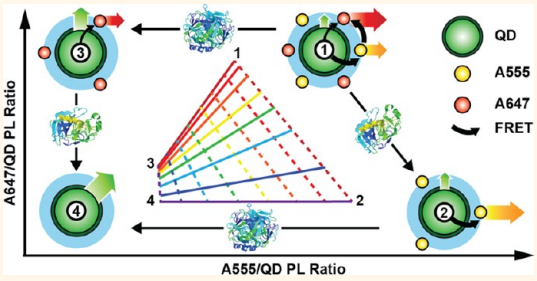

KEYWORDS: quantum dot · Förster resonance energy transfer · relay · multiplexing · peptide · protease · self-assembly

Semiconductor quantum dots (QDs) are one of the most promising and versatile nanomaterials available. Widespread interest in utilizing QDs for biological applications, such as multiplexed assays, imaging, sensing, and theranostics, is a result of their bright size-tunable photoluminescence (PL), small size, and surface area that can be chemically or biomolecularly tailored.[1−5] Within these applications, the combination of QDs with Förster resonance energy transfer (FRET) has been especially prominent.[6,7] To date, a myriad of FRET-based biosensing configurations have been developed for analytes as diverse as metabolites, drugs, ions, nucleic acids, and proteins, as well as the activity of enzymes such as proteases, nucleases, kinases, and oxidases.[3,6,7] FRET has also been used to signal the release of drug or DNA cargos from QD vectors in theranostic applications[2] and to drive the function of various biophotonic nanostructures based on QDs.[8,9] This breadth of research has been motivated by the unique optical properties of QDs, which are particularly suited for incorporation into energy transfer configurations. As FRET donors, their broad absorption spectra and/or large two-photon absorption cross sections allow for the selection of excitation wavelengths that minimize direct excitation of fluorescent dye acceptors. The spectrally narrow QD PL also helps maximize the spectral overlap integral while minimizing cross-talk between donor and

* Address correspondence to algar@chem.ubc.ca, igor.medintz@nrl.navy.mil.

Received for review October 12, 2012 and accepted November 24, 2012.

Published online December 05, 2012
10.1021/nn304736j

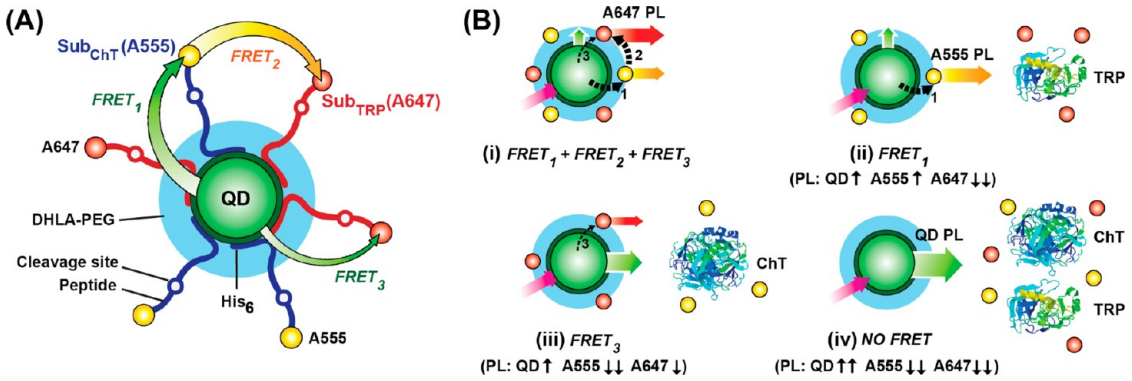

Figure 1. (A) Design of the concentric FRET relay and three possible energy transfer pathways between the QD, A555, and A647. The dye-labeled peptide substrates (Sub) are assembled to poly(ethylene glycol) ligand (DHLA-PEG)-coated CdSe/ZnS QDs *via* polyhistidine (His_6) tails. (B) Qualitative changes in PL from the three emitters as a function of trypsin (TRP) and chymotrypsin (ChT) activity. The sizes of the colored arrows reflect the magnitude of the PL intensities.

acceptor emission. Further, the nontrivial nanocrystal surface area permits tuning of energy transfer rates *via* the assembly of multiple acceptors around each donor. QDs can also be good FRET acceptors, most notably with chemiluminescent,[10,11] bioluminescent,[12,13] or photoluminescent lanthanide donors.[14,15] As acceptors, QDs offer very large spectral overlap integrals, long Förster distances, and excellent spectral separation between donor and acceptor emission.

Conventional FRET configurations with QD donors typically comprise an array of fluorescent dye[6,7] or protein acceptors[16,17] assembled around the central nanocrystal. Energy transfer is observed in a single step from the QD to one of the proximal acceptors. Even with multiple acceptors, the approximate centrosymmetry permits straightforward analysis of energy transfer rates and efficiencies *via* quenching of the QD PL and/or sensitization of the acceptor PL. This basic format is sufficient for many biological applications and is, by far, the most commonly reported in the literature. However, more complex configurations with additional energy transfer steps have also been reported.[8,18,19] For example, Medintz *et al.* devised a maltose sensing scheme where energy was transferred in two steps, first from a QD to a Cy3 dye label on a conjugated maltose binding protein (MBP), and then to a Cy3.5 dye associated with β-cyclodextrin bound by the MBP.[18] This FRET relay enabled efficient energy transfer over the >7.5 nm distance imposed by the radius of the QD and the dimensions of the MBP. Lu *et al.* studied a similar system where QDs were assembled with enhanced yellow fluorescent protein (EYFP) and, in turn, the EYFP was conjugated with an Atto-647 (acceptor)-labeled oligonucleotide.[19] In this example, the FRET relay extended the net range of energy transfer to a remarkable ~13 nm. Similarly, Boeneman *et al.* used a QD as an initial donor for an oligonucleotide-based, four-step photonic wire that had three relay dyes and a terminal dye along its >10 nm length.[8] The common feature of the above studies is that the FRET relays were designed to extend the range of energy transfer to distances greater than that allowed by the constraints of one-step FRET. Due to the greater number of emitters, analysis of these relay systems was more involved than conventional one-step FRET configurations but was simplified by treating each relay step as occurring between a discrete donor–acceptor pair. This approximation was reasonable since the intermediate and terminal acceptors were associated with the same biomolecular unit and directed excitation energy away from the central QD.

Here, we investigate the utility of a new FRET relay configuration that also uses a QD as an initial donor but, unlike previously reported relays,[8,18,19] is designed to be entirely concentric with the QD. This configuration is compact, such that the second energy transfer step neither moves the excitation energy any further away from the QD nor is limited to a discrete FRET pair attached to a common biomolecule. Rather, the concentric FRET relay comprises a central green-emitting CdSe/ZnS QD that has multiple Alexa Fluor 555 (A555) and Alexa Fluor 647 (A647) dyes assembled around it. As shown in Figure 1A, the dyes are distal labels on peptide substrates that are controllably self-assembled to the QD. Due to the spectral overlap between these dyes, energy transfer occurs from the QD to the A555 ($FRET_1$), from the A555 to the A647 ($FRET_2$), and, to a lesser extent, from the QD to the A647 ($FRET_3$). We first assemble varying numbers of A555-peptide and A647-peptide per QD and characterize the energy transfer efficiencies for $FRET_1$, $FRET_2$, and $FRET_3$. Analogous to conventional FRET configurations, the isolated $FRET_1$/$FRET_3$ pathways permit determination of the radial distance between the QD and A555/A647, respectively. In addition, the concentric design also allows us to use the $FRET_2$ pathway to infer the approximate distribution of self-assembled peptides across the QD surface, thereby addressing a question that has remained exceedingly challenging to date. Next, in a second set of experiments, we evaluate the potential for the concentric

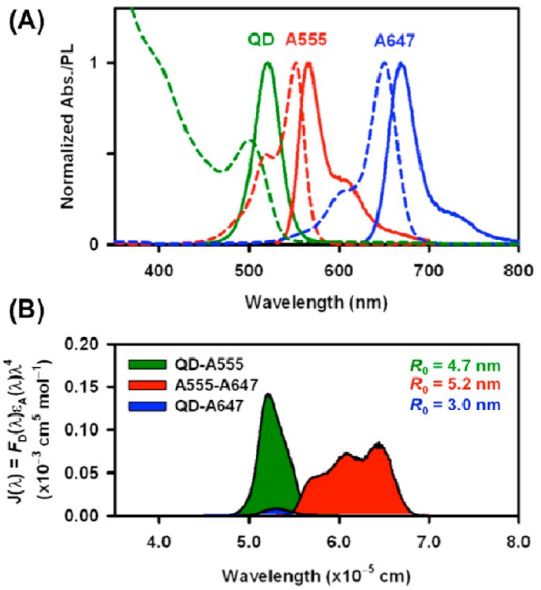

Figure 2. (A) Absorption (dashed lines) and emission (solid lines) spectra for the QD, A555, and A647. (B) Spectral overlap functions for the QD-A555, A555-A647, and QD-A647 FRET pairs. The Förster distances are also listed for each pair.

FRET relay to serve as a multiplexed probe for simultaneously sensing the activity of two proteases by selecting the peptides to be substrates for chymotrypsin (ChT) and trypsin (TRP). Figure 1B illustrates how changes in the relative QD, A555, and A647 PL intensities can be used to orthogonally track the activity of each protease. Importantly, the concentric FRET relay is also able to follow the TRP-catalyzed activation of inactive pro-chymotrypsin to ChT, demonstrating the potential for sensing coupled biochemical processes using one type of nanoparticle vector.

RESULTS AND DISCUSSION

Characterization of FRET Pairs. The concentric FRET relay comprised A555, A647, and CdSe/ZnS QDs with peak PL at 520 nm. Normalized absorption and emission spectra for each of these emitters are shown in Figure 2. The two primary FRET pairs within the relay were QD→A555 ($FRET_1$) and A555→A647 ($FRET_2$), where the arrow indicates the direction of energy transfer. The third FRET pair, QD→A647 ($FRET_3$), was much less efficient but nonetheless essential to multiplexed sensing (*vide infra*). Critical photophysical parameters for the three FRET pairs are summarized in Table 1. For a given donor–acceptor separation, the rate of $FRET_1$ was estimated to be 14 times faster than $FRET_3$ and thus was expected to be the dominant energy transfer pathway when both A555 and A647 were assembled to the same QD donor (see Supporting Information for the calculation). From the measured QD-A555 and QD-A647 distances (*vide infra*), the actual rate of $FRET_1$ was 10 times faster (per acceptor) than $FRET_3$.

TABLE 1. Photophysical Parameters Important to the Concentric FRET Relay

FRET pair[a]	Φ_D[b,c]	ε_A ($M^{-1}\ cm^{-1}$)[d]	J ($cm^6\ mol^{-1}$)[e]	R_0 (nm)[f]	r (nm)[g]
QD→A555 ($FRET_1$)	0.11	150000	5.21×10^{-10}	4.7	5.2
QD→A647 ($FRET_3$)	0.11	239000	3.76×10^{-11}	3.0	4.9
A555→A647 ($FRET_2$)	0.15	239000	6.68×10^{-10}	5.2	

[a] The arrow indicates the direction of energy transfer, donor (D)→acceptor (A). [b] Donor quantum yield (see Figure S1). [c] The manufacturer (Invitrogen) reports a quantum yield of 0.33 for A647. [d] Acceptor molar absorption coefficient (at absorption maximum). [e] Spectral overlap integral. [f] Förster distance. [g] Donor–acceptor separation for a centrosymmetric arrangement.

TABLE 2. Peptide Sequences

abbreviation	amino acid sequence[a]
Sub_{ChT}(A555)	(A555)C—SA**Y**AATDEGNQGT—SPPPPPPPS—HHHHHH
Sub_{TRP}(A647)	(A647)C—ST**R**TDEGNQGGTS—SPPPPPPPS—HHHHHH

[a] Peptides written N-terminal to C-terminal and shown in modular form: (1)-(2)-(3)-(4). Refer to the main text for a description of each module. The protease recognition sites are indicated in bold.

Peptides. The two peptide sequences used in this work are listed in Table 2. Each peptide included four functional modules: (1) an N-terminal cysteine residue that provided a unique site for labeling with maleimide-activated A555 or A647; (2) an extended amino acid sequence that incorporated a recognition site for a proteolytic enzyme; (3) a helical polyproline spacer; and (4) a C-terminal polyhistidine sequence used for assembly to QDs. Polyhistidine motifs enable spontaneous, rapid, and high-affinity ($K_d \sim 1$ nM) binding between peptides and the inorganic shell of CdSe/ZnS QDs.[20] One of the principal advantages of polyhistidine-mediated self-assembly is that the number of peptides per QD, or conjugate valence, can be controlled on the basis of relative stoichiometry.[20,21] Here, this was particularly important in assembling and tuning the concentric FRET relay around the QD. The polyproline spacer adjacent to the polyhistidine tail was expected to form a ~1.2 nm type-II helix[22] and help extend the recognition site away from the QD interface. The recognition site was chosen to render the peptide a substrate for one of two prototypical serine proteases: either TRP or ChT. TRP specifically cleaves C-terminal to Arg and Lys residues; ChT has much broader specificity but preferentially cleaves C-terminal to Phe, Trp, and Tyr residues.[23,24] The TRP substrate, Sub_{TRP}(A647), is an A647-labeled variant of a peptide we have previously used as a substrate in assays for TRP activity.[25,26] The sequence was modified to eliminate preferential cleavage sites for ChT. The ChT substrate, Sub_{ChT}(A555), was a similar peptide but incorporated an Ala-Tyr-Ala-Ala motif that Bizzozero *et al.* previously found to be optimal for ChT.[27] TRP and ChT were selected as model proteases since these enzymes are widely available,

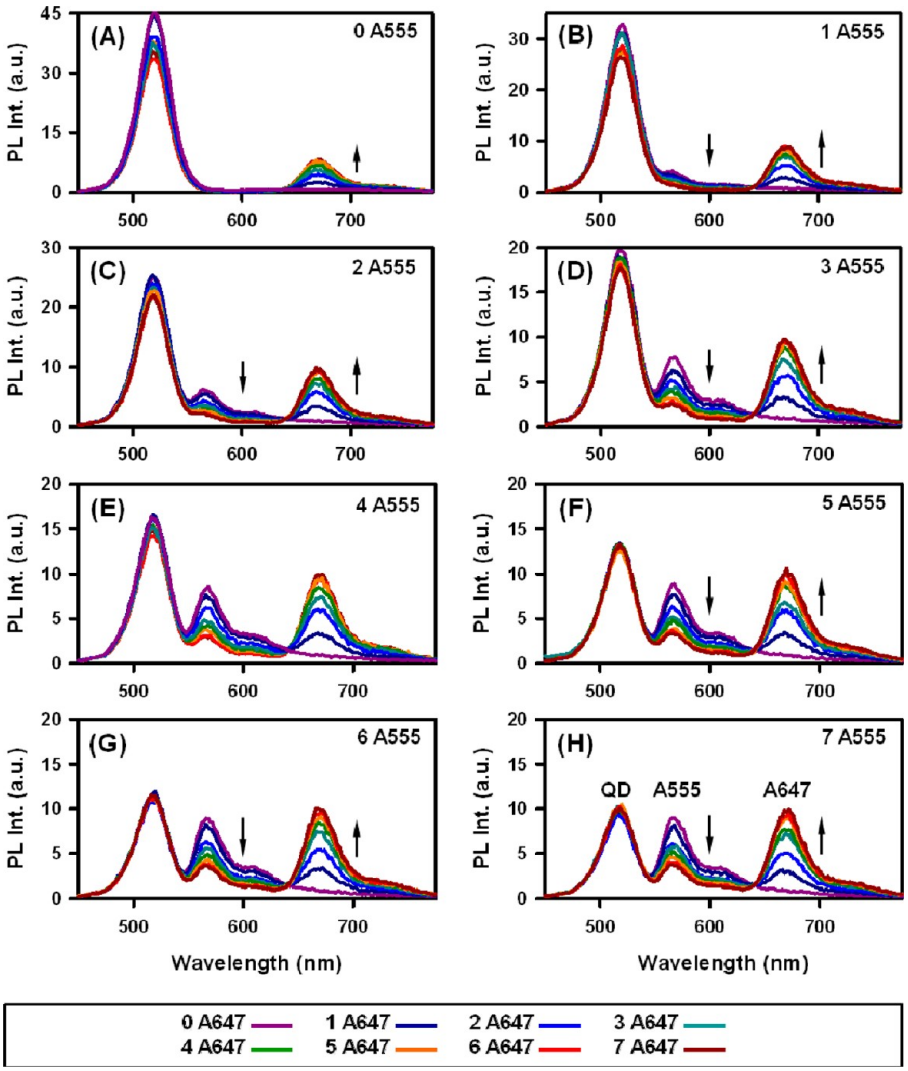

Figure 3. Ensemble PL spectra for $[Sub_{ChT}(A555)]_M$-QD-$[Sub_{TRP}(A647)]_N$ conjugates at values of $N = 0-7$ and (A–H) $M = 0-7$. Each panel corresponds to a unique value of M, the number of A555 per QD. The arrows indicate the trends in PL as N, the number of A647 per QD, increased. The QD, A555, and A647 PL contributions are labeled in panel (H). Note that the scale of the y-axis changes from (A) to (H). The excitation wavelength was 400 nm. A single plot with $M = 0-7$ for $N = 0$ is shown in the Supporting Information, Figure S3.

well-known, and extensively characterized and exhibit robust hydrolytic activity.[28] Analogous to previous use of MBP as a model protein,[18] TRP and ChT have been frequently used for prototyping new QD-based biosensing configurations in the context of proteolytic activity.[25,29,30]

Assembly of the Concentric FRET Relay. The concentric FRET relay was assembled by mixing $M = 0-7$ equiv of Sub_{ChT}(A555) with QDs, then incrementally adding $N = 0-7$ equiv of Sub_{TRP}(A647) in a second step. This procedure resulted in 64 distinct configurations with varying degrees of $FRET_1$, $FRET_2$, and $FRET_3$. The PL spectra for each configuration are shown in Figure 3 and grouped according to the average number (M) of A555 assembled. Direct excitation of both the A555 and A647 was negligible (see Figure S2), and several trends in the FRET-sensitized PL are worth noting. First, the QD PL decreased as the number of proximal A555 increased. This observation was consistent with an increasing rate of $FRET_1$ (compare QD PL across Figure 3A–H). In the absence of A555 (Figure 3A; $M = 0$), increases in the number (N) of proximal A647 yielded progressive quenching of QD PL *via* $FRET_3$. The magnitude of quenching was considerably less than that observed with $FRET_1$, congruent with the lower rate of $FRET_3$ per unit distance and the approximately equal lengths of Sub_{ChT}(A555) and Sub_{TRP}(A647). However, as the number of A555 per QD increased, there was a progressive decrease in $FRET_3$-induced quenching of QD PL until becoming negligible at $M \geq 4$ A555 per QD (*i.e.*, no significant decrease in the QD PL intensity with increasing A647 per QD in Figure 3F–H). This trend reflected the nearly complete dominance of the $FRET_1$ over $FRET_3$ when A555 was not outnumbered by co-assembled A647. Such behavior was expected based on eq 1, the net energy transfer efficiency for the QD donor, E_{1+3}, where k_3 is the rate of $FRET_3$, $k_1 \approx 10k_3$ is

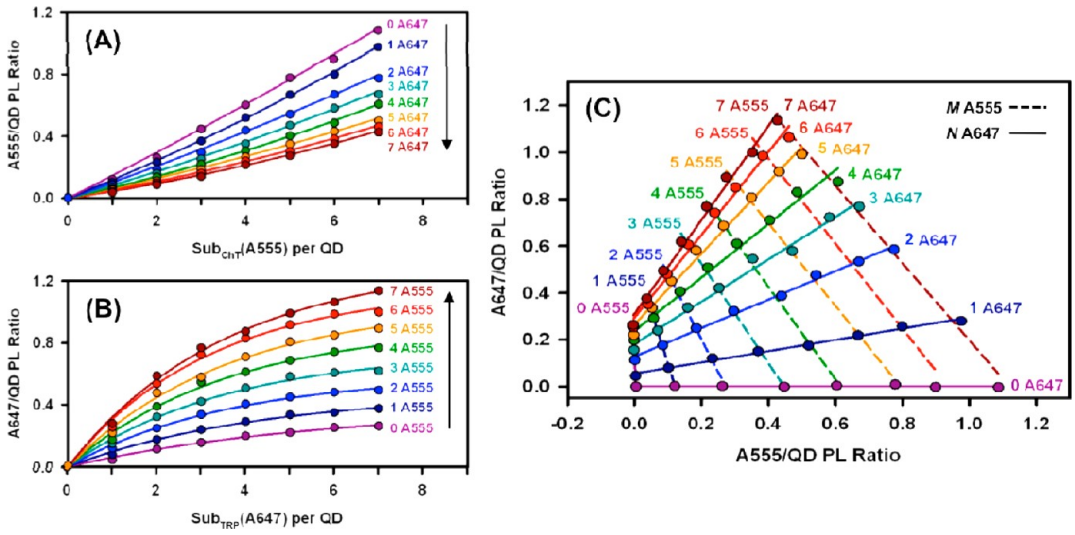

Figure 4. Changes in (A) the A555/QD PL ratio and (B) the A647/QD PL ratio as a function of the average number of Sub$_{ChT}$(A555), *M*, and Sub$_{TRP}$(A647), *N*, per QD. (C) A647/QD PL ratios plotted *versus* A555/QD PL ratios. Each combination of PL ratios (*i.e.*, point on the plot) corresponds to a unique combination (*M*,*N*).

the rate of FRET$_1$, and k_0 is the sum of the radiative and nonradiative relaxation rates for the QD donor. Note that FRET$_2$ is excluded from this expression because it occurs subsequent to FRET$_1$ and does not involve the QD.

$$E_{1+3}(M,N) = 1 - \frac{I_{QD}(M,N)}{I_{QD}(0,0)} = \frac{Mk_1 + Nk_3}{Mk_1 + Nk_3 + k_0} \quad (1)$$

Considering A555 and A647, the FRET$_1$-sensitized A555 PL increased in parallel with the number of A555 assembled per QD (compare A555 PL across Figure 3A–H; FRET$_1$ efficiency increases). An analogous trend was observed in the FRET$_3$-sensitized A647 PL (Figure 3A). When A555 and A647 were co-assembled to the QDs, the FRET$_1$-sensitized A555 PL decreased as a function of the number of A647 due to greater rates of FRET$_2$. Parallel increases in FRET$_2$-sensitized A647 PL were also observed. These trends are shown in Figure 4A,B, which plot the A555/QD and A647/QD PL ratios (derived using eqs 2–6; see Materials and Methods) as functions of the number of A555 and A647 per QD, respectively. The data clearly show the FRET$_1$–FRET$_2$ relay and its "push-pull" effect on the magnitude of the A555 PL. Figure 4C plots the A647/QD PL ratio as a function of the A555/QD and reveals that each of the 64 FRET relay configurations (*M*,*N*) had a unique coordinate in this two-dimensional space. This was an important result that we later exploited for multiplexed sensing in kinetic assays for protease activity (*vide infra*).

FRET$_1$ and FRET$_3$ Efficiency and Radial Distance Measurements. In addition to the acceptor/donor PL ratios for the FRET configurations, we also calculated the FRET efficiencies. For FRET relay configurations with only A555 assembled ($M = 0–7$, $N = 0$), the FRET$_1$ efficiency was calculated from the quenching of the QD PL (eq 7; see Materials and Methods). Similarly, the FRET$_3$ efficiency was calculated from the quenching of the QD PL

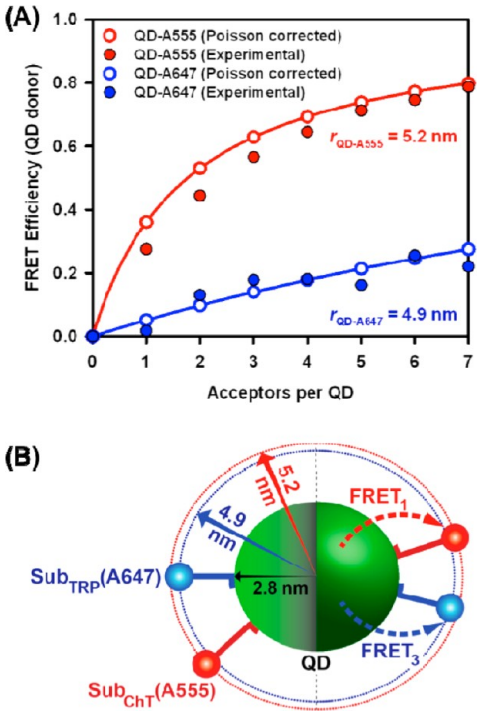

Figure 5. (A) Changes in FRET efficiency as a function of the number of acceptors assembled per QD for the QD-A555 ($M = 0–7$, $N = 0$) and QD-A647 ($M = 0$, $N = 0–7$) FRET pairs. The Poisson corrected data are shown in parallel with the raw data. (B) Illustration of the concentric spheres upon which A555 and A647 are positioned (on average). A few of each dye are shown at random positions on the spheres. The diameter of the QD is 5.6 nm.[32]

when only A647 was assembled ($M = 0$, $N = 0–7$). These results are shown in Figure 5A with and without a correction that accounts for the Poisson distribution (*i.e.*, heterogeneity) in the number of Sub$_{ChT}$(A555) or Sub$_{TRP}$(A647) assembled per individual QD, across the ensemble (eq 8; see Materials and Methods).[31] The net

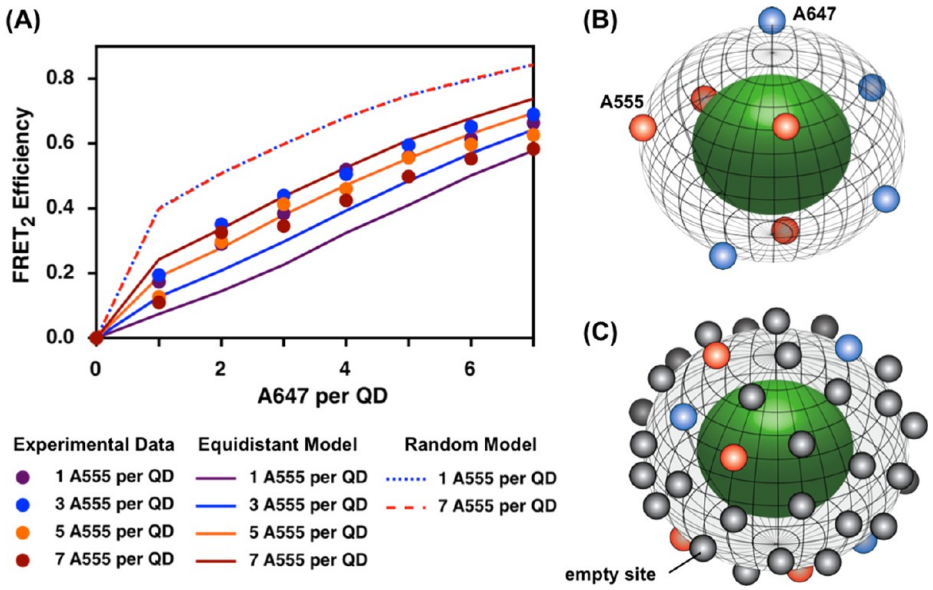

Figure 6. (A) Experimental and modeled $FRET_2$ efficiencies as a function of the number of A647 per QD, *N*, and the number of A555 per QD, *M*. The random model data for 1 A555 and 7 A555 per QD overlap (as do intermediate values). (B) Schematic example of the positions of 4 A555 (red) and 4 A647 (blue) dye positions in the equidistant model. (C) Schematic example of 4 A555 (red) and 4 A647 (blue) dye positions in the random model. The remaining unoccupied binding sites are also shown (gray). The background of the dye sphere is opaque for clarity and hides some of the 50 total binding sites.

effect of this population heterogeneity is a nontrivial decrease in the *apparent* FRET efficiency at acceptor valences less than *ca.* 4 per QD.[31] The correction allowed for a more accurate calculation of the donor–acceptor separations from the measured ensemble FRET efficiencies. Center-to-center separations for the QD-A555 and QD-A647 FRET pairs were 5.2 and 4.9 nm, respectively, as shown in Figure 5B. The close agreement of these values was consistent with the equal number of amino acid residues between Sub_{ChT}(A555) and Sub_{TRP}(A647). This result also suggested that the A555 and A647 were co-situated on the surface of a figurative ~10 nm diameter sphere with the QD at its center (*i.e.*, the dye sphere reflecting the position of the acceptors was concentric with the QD).

$FRET_2$ Efficiency and Peptide Arrangement. The other pertinent FRET efficiency was that for $FRET_2$ between A555 and A647. For a fixed number of A555 per QD (*M*), the efficiency was calculated from the quenching of the A555 PL (eq 7) as the number of proximal A647 (*N*) increased. The data are shown in Figure 6A as a function of *N* for each set of *M* = 1, 3, 5, 7 (complete data for *M* = 1–7 are shown in Figure S4). The $FRET_2$ efficiency increased as the number of A647 per QD increased and, in general, decreased slightly as the number of A555 per QD increased. It is important to note that $FRET_2$ was not in competition with $FRET_3$. If the QD transferred its energy to A647 *via* $FRET_3$, then A555 was not excited *via* $FRET_1$ and $FRET_2$ did not subsequently occur. If the QD transferred its energy to A555 *via* $FRET_1$, then A647 was not excited *via* $FRET_3$ and all A647 were good acceptors for $FRET_2$. The negligible direct excitation of A555 and A647 was important for achieving this mutually exclusive nature for $FRET_2$ and $FRET_3$. Furthermore, it must also be noted that $FRET_2$ in these configurations did not comprise a multiple donor–multiple acceptor system. Although there were multiple A555 per QD, the QD was only able to sensitize *one* A555 dye molecule, *via* $FRET_1$, per excitation event. The remaining ground state A555 were not donors, and thus this second FRET system was a one donor (A555)–multiple acceptor (A647) arrangement, where the various donor–acceptor separations were, to a first approximation, different chords of a ~10 nm diameter sphere (*vide supra*). Since this configuration was not centrosymmetric, it was neither straightforward to calculate the average A555–A647 separation distance nor physically relevant. Nonetheless, the $FRET_2$ efficiency as a function of *M* and *N* was expected to provide insight into the interfacial arrangement of polyhistidine-appended peptides self-assembled onto the QDs, which has been of general interest but difficult to address due to the lack of adequate tools. We therefore considered two limiting models for the assembly of Sub_{ChT}(A555) and Sub_{TRP}-(A647) to QDs. The first "equidistant" model hypothesized that, at equilibrium, the peptides arranged themselves to be equidistant on the three-dimensional surface of the QD, as far from one another as possible, and that this arrangement was mirrored by the A555 and A647 dye labels. The second "random" model instead hypothesized that the QD had a set number of fixed binding sites that the peptides occupied stochastically. The number of binding sites was chosen to correspond to the results of a recent study that found a maximum of 50 ± 10 peptides were able to

assemble to QDs of this size.[33] Thus, 50 equally favored, evenly spaced interfacial binding sites were posited in this second model and also assumed to be reflected by the positioning of the A555 and A647 labels. The assumption that the dye positions reflect the binding site positions is valid if each individual peptide has a similar, time-averaged conformation when bound to different sites at the QD interface.

Figure 6B shows an example of the equidistant model with 8 peptides/dyes assembled per QD (4 A555 and 4 A647 in the illustration). Of the 64 different permutations of $M = 0-7$ and $N = 0-7$, a configuration with 8 total peptides/dyes is most probable (*i.e.*, x A555 and $8-x$ A647). Figure 6C shows an analogous example of the random model, along with the 42 unoccupied sites that remain. For both models, the distances between an arbitrary A555 donor and co-assembled A647 acceptors were calculated, averaged over a large ensemble (including a Poisson distribution of valences), and used to determine the expected $FRET_2$ efficiency for each (*M*,*N*) configuration using the parameters in Table 1. The results are shown in Figure 6A, where the random model has a notably higher $FRET_2$ efficiency than the equidistant model. This is because, in the random model, peptides/dyes have the opportunity to assemble very close to one another, regardless of the total number of assembled peptides. In contrast, the equidistant model ensures that peptides/dyes are as far apart as possible. Given the strong distance dependence of FRET, the outcome is a $FRET_2$ efficiency in the random model that can be *ca.* 10−40% higher than the equidistant model depending on the (*M*,*N*) configuration. As expected, the $FRET_2$ efficiency in the random model is independent of *M*, the number of A555 per QD, since there is only one excited state donor. Further considering the uncertainty in the maximum number of binding sites per QD, adjusting the random model for 40 or 60 peptides per QD (*i.e.*, 50 ± 10 peptides)[33] does not significantly change the random model data shown in Figure 6 (see Supporting Information, Figure S5).

The experimental data in Figure 6A most closely resemble the equidistant assembly model, falling within the same range of $FRET_2$ efficiencies. The experimental efficiencies are clearly too low to correlate with the random assembly model. In order for the predicted efficiencies for the random model to begin to approach those for the equidistant model, there would have to be a maximum of ~20 binding sites per QD, which is not consistent with experimental results.[33] Even in such a scenario, the initial rise in the experimental $FRET_2$ efficiency with increasing A647 per QD is much slower than predicted for random assembly (see Supporting Information, Figure S5). The agreement between the data and the equidistant model was not complete, however, as the trends in $FRET_2$ efficiency as a function *M* and *N* deviated somewhat from those predicted. For example, the spread in the data between $M = 1-7$ was smaller than predicted, and the observed trend—a decrease in $FRET_2$ efficiency between $M = 1$ and $M = 7$—was opposite that predicted. There are several possible reasons for the departures from the ideal equidistant model. One initial hypothesis was that homo-FRET (*i.e.*, energy transfer between excited state A555 and proximal ground state A555) was decreasing the experimental $FRET_2$ efficiency as the number of A555 per QD increased; however, inclusion of homo-FRET in the random and equidistant models (see Supporting Information, Figure S6) did not reproduce the observed trend: there was almost no effect in the equidistant model, and in the random model, the effect of homo-FRET slightly increased the predicted $FRET_2$ efficiency (see Figure S6). Other possibilities for the discrepancies between the equidistant model and experimental data are nonidealities in the real system. For example, real QDs are not spheres but are rather faceted nanocrystals, and this more complex geometry will change the distances between A555 and A647 dye molecules. Further, different facets of the QD are not chemically equivalent, and the polyhistidine tails of the peptides may have different affinities for each. Equidistant and equally favored binding sites are thus simplifying assumptions. The fluorescence properties of the A555 may also change as more peptides are assembled per QD, similar to the self-quenching frequently observed as the degree of labeling for a protein increases.[34] This latter effect would certainly decrease the $FRET_2$ efficiency. Although the equidistant model is not a complete description of the QD−peptide conjugates, it appears to be a reasonable first approximation for the binding of peptides to QDs, averaged over both time and the ensemble. The two-step assembly process used in our experiments is not expected to have any significant effect on these results (see Supporting Information, Figure S7, for discussion). Note that our model and data do not say how the peptides achieved the equidistant configuration, whether *via* initial binding or by subsequent migration over the surface of the QD as equilibrium was approached.

Sensing Proteolytic Activity. Given that each unique combination of A555 and A647 per QD, (*M*,*N*), yielded a unique combination of A555/QD and A647/QD PL ratios, (ρ_{A555}, ρ_{A647}) (see Figure 4C), we hypothesized that the concentric FRET relay assembly could be used for multiplexed protease assays. It was possible to investigate this possibility since the A647- and A555-labeled peptides were designed to be substrates for trypsin (TRP) and chymotrypsin (ChT), respectively. Proteolytic activity was expected to progressively change (*M*,*N*), resulting in changes in the A555/QD and A647/QD PL ratios, (ρ_{A555}, ρ_{A647}), that could be tracked in real time and thus permit quantitative measurement of hydrolytic rates. Experimentally, the

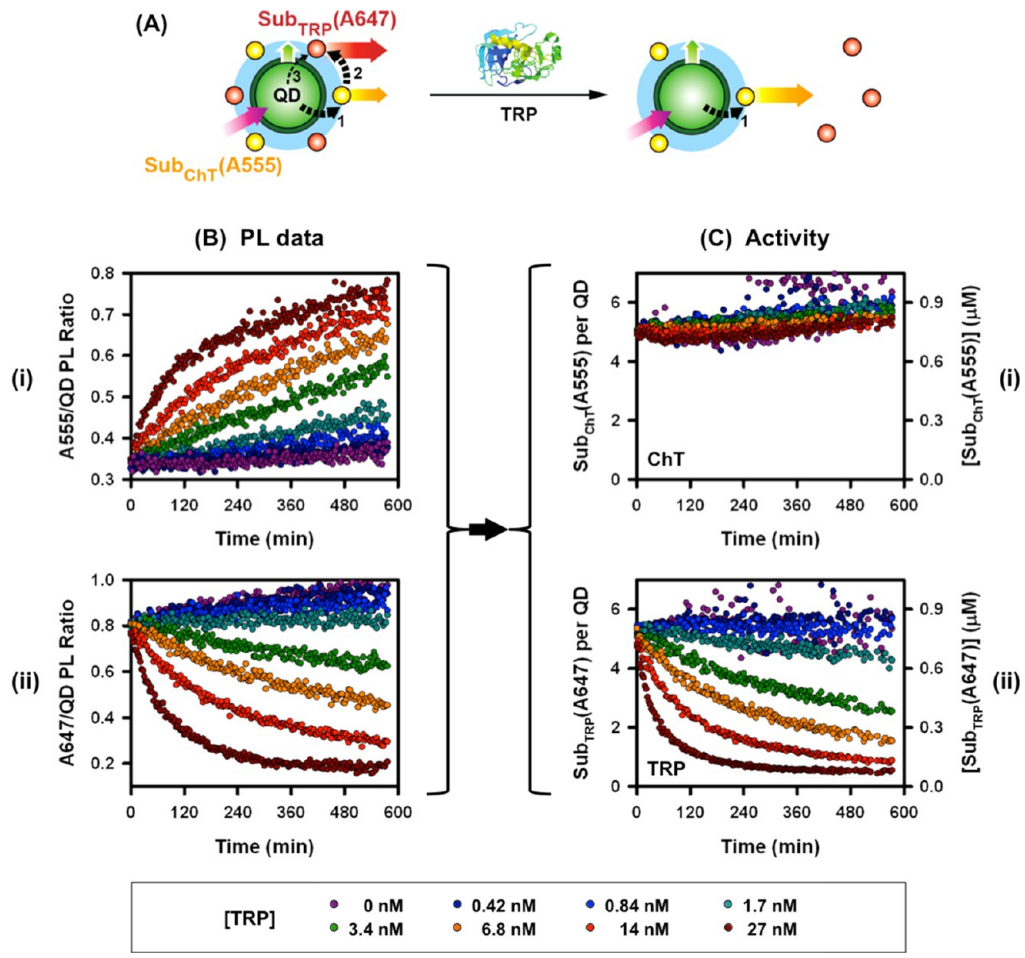

Figure 7. (A) Schematic of the TRP sensing experiment with FRET$_1$, FRET$_2$, and FRET$_3$ indicated by 1, 2, and 3, respectively. (B) (i) A555/QD and (ii) A647/QD PL ratios and (C) corresponding activity data for the digestion of (i) Sub$_{ChT}$ and (ii) Sub$_{TRP}$ in [Sub$_{ChT}$(A555)]$_5$-QD-[Sub$_{TRP}$(A647)]$_5$ conjugates by different concentrations of TRP. The combined PL data (B,i-ii) are utilized to calculate the progress curves (C,i-ii).

changes in (ρ_{A555}, ρ_{A647}) were measured by tracking changes in the PL intensity at 530, 570, and 670 nm. To a first approximation, these wavelengths corresponded to PL from the QD, A555, and A647, respectively (see Materials and Methods for cross-talk corrections). Three different protease sensing experiments are described below.

Trypsin Assay. The concentric FRET relay was first tested for sensing applications in a proteolytic assay for TRP activity (Figure 7A). Nominal [Sub$_{ChT}$(A555)]$_5$-QD-[Sub$_{TRP}$(A647)]$_5$ conjugates (0.15 μM) were mixed with different concentrations of TRP (0.42−27 nM), and the PL intensities at 520, 570, and 670 nm were tracked over time in a progress curve format.[32] The expectation was that TRP activity would convert the conjugates to [Sub$_{ChT}$(A555)]$_5$-QD with loss of FRET$_2$/FRET$_3$ sensitization of A647 PL. The experimental, time-dependent changes in each PL channel are shown in the Supporting Information (Figure S8). A555/QD and A647/QD PL ratios were calculated from these data and are shown in Figure 7B. In the presence of TRP, the A555/QD PL ratio increased and the A647/QD PL ratio decreased, in agreement with expectations for the loss of FRET$_2$/FRET$_3$. Importantly, the rate of these changes scaled proportionally to the concentration of TRP. The PL data were converted to activity data by mapping the time-dependent (A555/QD, A647/QD) PL ratios to (*M*,*N*) coordinates using the calibration data set in Figure 4. The resulting progress curves for ChT and TRP activity are shown in Figure 7C. As expected, the rate of digestion of Sub$_{TRP}$(A647) increased with increasing concentrations of TRP, whereas Sub$_{ChT}$(A555) was not appreciably digested due to the absence of ChT. The few points dispersed about the progress curves for the negative controls in Figure 7C are artifacts of the mathematical conversion from (A555/QD, A647/QD) PL ratios to (*M*,*N*).

Trypsin and Chymotrypsin Assay. The sensing capability of the concentric FRET relay was next tested in a multiplexed assay with both TRP and ChT (Figure 8A). The TRP concentration was varied as before (0.42−27 nM), while the concentration of ChT was held constant (40 nM). The expectation was that the combined activity of TRP and ChT would convert the [Sub$_{ChT}$(A555)]$_5$-QD-[Sub$_{TRP}$(A647)]$_5$ conjugates (0.15 μM) to QDs with loss

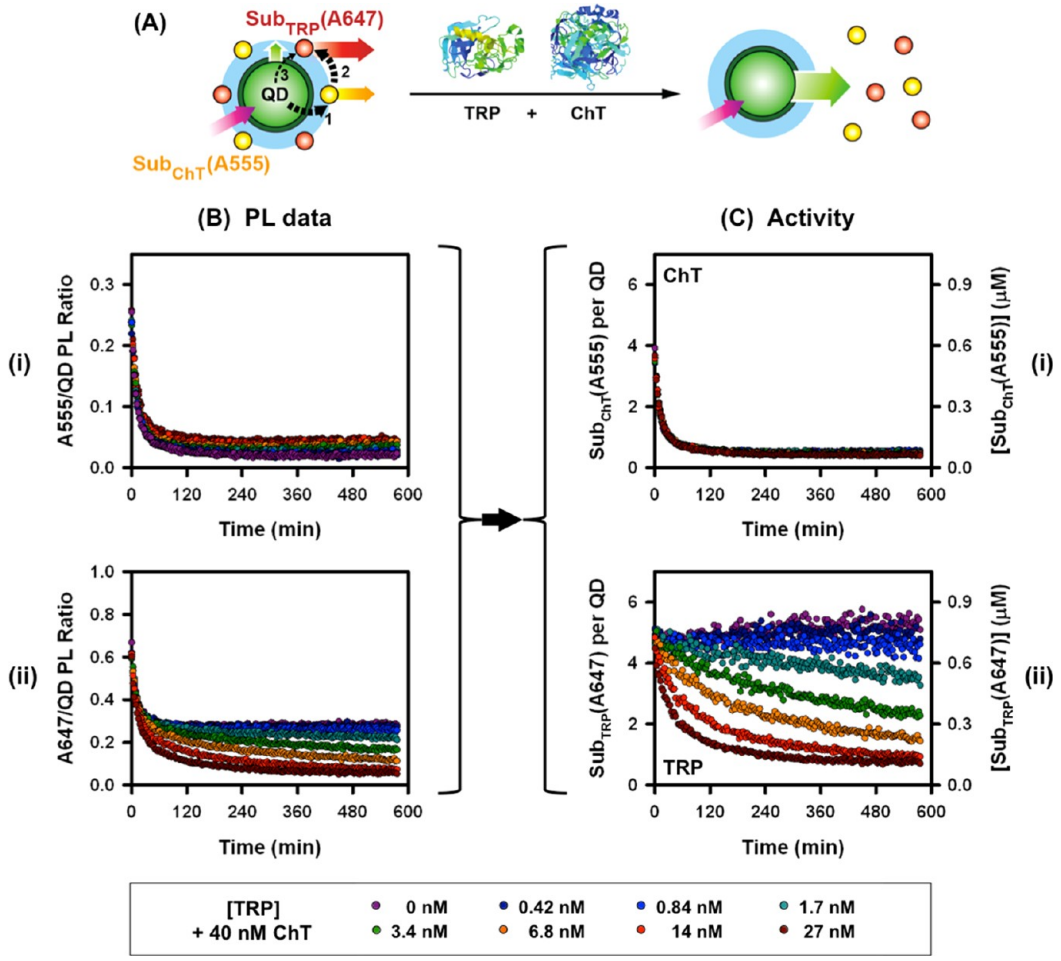

Figure 8. (A) Schematic of the TRP + ChT sensing experiment with $FRET_1$, $FRET_2$, and $FRET_3$ indicated by 1, 2, and 3, respectively. (B) (i) A555/QD and (ii) A647/QD PL ratios and (C) corresponding activity data for the digestion of (i) Sub_{ChT} and (ii) Sub_{TRP} in $[Sub_{ChT}(A555)]_5$-QD-$[Sub_{TRP}(A647)]_5$ conjugates by different concentrations of TRP + 40 nM ChT. The combined PL data (B,i-ii) are utilized to calculate the progress curves (C,i-ii).

of both $FRET_1$-sensitized A555 PL and $FRET_2$/$FRET_3$-sensitized A647 PL.

The experimental, time-dependent changes in the PL intensities at 520, 570, and 670 nm are shown in the Supporting Information (Figure S9), and the corresponding changes in the A555/QD and A647/QD PL ratios are shown in Figure 8B. The A555/QD PL ratio rapidly decreased to the baseline, as expected for ChT activity. A similarly rapid decrease was observed with the A647/QD PL ratio, except that the end point depended on the concentration of TRP. At 0 nM TRP, the end point was *ca.* 0.3 but gradually approached the baseline as the concentration of TRP increased to 27 nM. The rapid decreases in both progress curves corresponded to loss of $FRET_1$ and $FRET_2$ with ChT activity and rapid digestion of Sub_{ChT}(A555). The decreasing end point for the A647/QD PL ratio corresponded to retention or loss of $FRET_3$ (and residual A647 PL) depending on TRP activity and the rate of digestion of Sub_{TRP}(A647). A close examination also shows that the A555/QD PL ratio was somewhat dependent on the concentration of TRP, exhibiting a slower decrease as the concentration of TRP increased due to different rates of loss of $FRET_2$ with digestion of Sub_{TRP}(A647). Progress curves (*M*,*N*) for combined ChT and TRP activity were calculated from PL ratios (A555/QD, A647/QD) as noted previously and are shown in Figure 8C. Regardless of the TRP concentration, the progress curves for the digestion of Sub_{ChT}(A555) followed a common trajectory, as expected for a fixed concentration of ChT. In contrast, a series of progress curves were observed for the digestion of Sub_{TRP}(A647) with rates proportional to the concentration of TRP.

Activation of Chymotrypsinogen by Trypsin. The final sensing configuration tested was the activation of chymotrypsinogen (pro-ChT) to ChT (Figure 9A). Nominal $[Sub_{ChT}(A555)]_5$-QD-$[Sub_{TRP}(A647)]_5$ conjugates (0.15 μM) were mixed with 39 nM pro-ChT and varying concentrations of TRP (0.42−27 nM). The expectation was that the activity of TRP would have two effects: (1) TRP-catalyzed digestion of the full conjugates to $[Sub_{ChT}(A555)]_5$-QD with loss of $FRET_2$/$FRET_3$; and (2) conversion of the pro-ChT to ChT with subsequent digestion of $[Sub_{ChT}(A555)]_5$-QDs to only QDs with loss

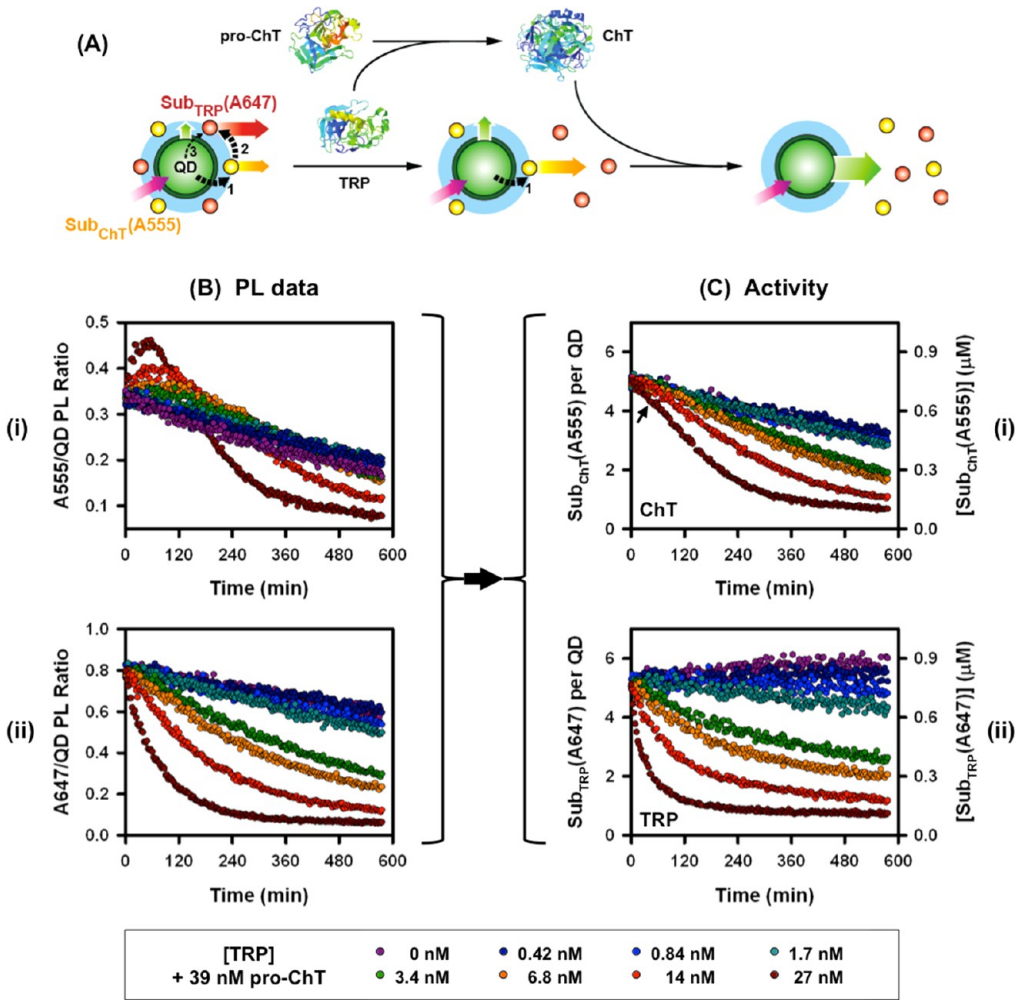

Figure 9. (A) Schematic of the pro-ChT activation sensing experiment with $FRET_1$, $FRET_2$, and $FRET_3$ indicated by 1, 2, and 3, respectively. (B) (i) A555/QD and (ii) A647/QD PL ratios and (C) corresponding activity data for the digestion of (i) Sub_{ChT} and (ii) Sub_{TRP} in $[Sub_{ChT}(A555)]_5$-QD-$[Sub_{TRP}(A647)]_5$ conjugates by different concentrations of TRP + 39 nM pro-ChT. The combined PL data (B,i-ii) are utilized to calculate the progress curves (C,i-ii). The arrow in (C,i) indicates the approximate inflection point. Digestion of Sub_{ChT}(A555) did not reach completion within the 10 h duration of the experiment.

of $FRET_1$. Therefore, changes in $FRET_1$ were expected to lag behind changes in $FRET_2$/$FRET_3$ and yield an initial period of increase in the A555/QD PL ratio that was followed by a period of decrease.

The experimental, time-dependent changes in the PL signals at 520, 570, and 670 nm are shown in the Supporting Information (Figure S10); the corresponding changes in the A555/QD and A647/QD PL ratios are shown in Figure 9B. The different combinations of TRP + pro-ChT produced trends that were clearly different than those observed with TRP alone or TRP + ChT. In samples with only pro-ChT (no TRP), the A647/QD PL ratio decreased (Figure 9B,ii) but did so at a much slower rate than observed with an equivalent concentration of ChT (Figure 8B,ii). Similarly, the A555/QD PL ratio exhibited only a slow decrease (Figure 9B,i). Both of these results were consistent with minimal activity for the putatively inactive pro-ChT (*cf.* ChT in Figure 8) and much slower loss of $FRET_1$ and $FRET_2$. As the concentration of TRP increased, the time-dependent A647/QD PL decreased at a progressively faster rate, which was consistent with the expected loss of $FRET_2$/$FRET_3$ with digestion of Sub_{TRP}(A647). Importantly, the A555/QD PL ratio exhibited the expected nonmonotonic behavior as the concentration of TRP increased in the presence of pro-ChT: there was (1) an initial increase, consistent with the loss of $FRET_2$ due to TRP activity and digestion of Sub_{TRP}(A647), followed by (2) a turning point and decrease, consistent with the loss of $FRET_1$ due to delayed ChT activity and digestion of Sub_{ChT}(A555). These results were clear indications of the TRP-catalyzed activation of pro-ChT to ChT.

Progress curves (*M*,*N*) for combined ChT and TRP activity were again calculated from PL ratios (A555/QD, A647/QD) and are shown in Figure 9C. The progress curves for the digestion of Sub_{TRP}(A647) (Figure 9C,ii) were analogous to those for equivalent concentrations of TRP alone (Figure 7C,ii) or in the presence of ChT (Figure 8C,ii). In contrast, the progress curves for the digestion of Sub_{ChT}(A555) (Figure 9C,i) were distinctly

TABLE 3. Comparison of the Specificity Constants (k_{cat}/K_m) for Each Concentration of TRP Used in the Three Protease Assays with the Concentric FRET Relay

	k_{cat}/K_m (s^{-1} mM^{-1})				
[TRP] (nM)	3.4	6.8	14	27	ave.[a]
TRP	8.1	14.3	12.4	14.2	12 ± 3
TRP + ChT[b]	24.3	20.4	19.1	13.9	19 ± 4
TRP + pro-ChT[c]	7.9	10.8	14.1	17.9	13 ± 4

[a] One standard deviation is reported. [b] 40 nM ChT. [c] 39 nM pro-ChT. Lower concentrations of TRP did not provide sufficient activity for fitting specificity constants.

different than those observed with ChT (Figure 8B,i). The slow decrease in Sub_{ChT}(A555) per QD in the absence of TRP was attributed to background ChT-like activity in the pro-ChT sample. At higher concentrations of TRP, the progress curves were characterized by a time lag relative to both the parallel TRP activity (Figure 9C,ii) and previous experiments with similar ChT concentrations (Figure 8C,i). An inflection point was also observed before the progress curve approached the baseline. These results were consistent with expectations for the activation of pro-ChT to ChT. Nonetheless, we sought to validate the general shape of the Sub_{ChT}(A555) progress curves using standard fluorogenic substrates for TRP and ChT, N_α-benzoyl-DL-arginine-2-naphthylamide hydrochloride (BANA)[35] and Ala-Ala-Phe-7-amido-4-methylcoumarin (AAF-MCA),[36] respectively. Importantly, similar lags, inflection points, and background pro-ChT activity were observed for the digestion of AAF-MCA by mixtures of TRP and pro-ChT (see Supporting Information, Figures S11–S14). This congruence between the QD-FRET and AFF-MCA/BANA assay formats confirmed that the concentric FRET relay was suitable not only for multiplexed detection but also for quantitatively tracking coupled enzyme activity.

Specificity Constants. The progress curves for the tryptic digestion of Sub_{TRP}(A647) (Figure 7C–9C) were fit with an integrated Michaelis–Menten (MM) model (see Supporting Information for details, Figure S15) to extract specificity constants, $(k_{cat}/K_m)_{TRP}$, which are listed in Table 3. The specificity constant for ChT activity toward Sub_{ChT}(A555) was $(k_{cat}/K_m)_{ChT}$ = 24 s^{-1} mM^{-1} (see Figure 8). The $(k_{cat}/K_m)_{TRP}$ values are used to compare between data sets and, importantly, to demonstrate the capacity for quantitative sensing of proteolytic activity using the concentric FRET relay. The specificity constants between TRP and TRP + pro-ChT assays were generally in good agreement; however, in the ChT assay, particularly at lower TRP concentrations, the measured specificity constant tended to be higher than the other two formats. This was attributed to the broader specificity of ChT and some cross-reactivity with Sub_{TRP}(A647). Even with this effect, the average values of k_{cat}/K_m for each assay format were in agreement within the precision of the experiment (±1 standard deviation), thus confirming the capability for quantitative, multiplexed analysis of protease activity using the concentric FRET relay. The measured values for k_{cat}/K_m are comparable to those of commercially available assays kits, which span a broad range from 0.4 to 150 s^{-1} mM^{-1}.[37]

Discussion and Conclusions. We have used a concentric FRET relay to (i) investigate the physical assembly of peptides to a QD and (ii) demonstrate multiplexed sensing of proteolytic activity. To date, the predominant use of FRET relays has been to extend the range of energy transfer over longer distances. Our work here greatly expands the utility of FRET relays assembled with an initial QD donor, as we discuss below.

FRET is well-known for its "molecular ruler" capability[38] and can be used to physically characterize nanoparticles and their bioconjugates. The typical length scale of FRET (1–10 nm)[39] provides distance information that is complementary to electron microscopy, which tends to characterize only the inorganic component of nanoparticles, and to light scattering techniques, which estimate hydrodynamic size. For example, FRET from a QD donor to dye acceptor has been used to determine the orientation of proteins[40] and oligonucleotides[41,42] conjugated to QDs and to track the dynamic conformational switching of single Holliday junctions bound to a QD.[43] Recently, Morgner *et al.* used a time-resolved analysis of FRET between luminescent terbium complex (LTC) donors and QD acceptors to measure asymmetry in the shape of QDs, including the long- and short-axis dimensions.[39] The common aspect between these studies is that the measured donor–acceptor distances were effectively radial. Methods to obtain insight into the interfacial arrangement of biomolecules assembled to QDs have been largely overlooked and unknown in almost all previous studies that use FRET to characterize QD bioconjugates. Our use of a concentric FRET relay in conjunction with modeling of the expected energy transfer in two putative arrangements of dye-labeled peptides (random *vs* equidistant) provided insight into this complex question. The modeled and experimental data indicated that assembling a total number of peptides less than the surface capacity of the QD (<30%) results in nonrandom placement of those peptides and some degree of preference for maximizing interpeptide spacing. More sophisticated modeling and further development of the concentric FRET technique (*e.g.*, time-resolved analysis and/or the introduction of an additional relay step such as QD→A555→A647→Alexa Fluor 750) may permit resolution of nonrandom, nonequidistant interfacial arrangements of biomolecules assembled to a common QD, taking into account nonspherical shapes and potential facet preferences.

The second novel aspect of this work is demonstration of the multiplexed detection of the activity of two different proteases, using one QD assembly, *via* the concentric FRET relay. The current state-of-the-art for multiplexing with QDs and FRET is the use of *N* different colors of QD, as components of *N* different FRET pairs, to detect *N* different bioanalytes. Examples include the detection of two different oligonucleotide targets using green-emitting QDs paired with a Cy3 dye acceptor and red-emitting QDs paired with an A647 acceptor;[44] activity-profiling of two proteases using two colors of QD acceptor paired with a common bioluminescent protein donor;[13] parallel detection of a kinase and protease using two colors of QD donors paired with Alexa Fluor 660 and gold nanoparticle (Au NP) acceptors;[45] and the concurrent detection of cocaine and adenosine using aptamers coupled to two different colors of QD and quenched by Au NPs.[46] Our demonstration of the multiplexed detection of TRP and ChT activity, as well as the activation of pro-ChT by TRP, using *one* QD assembly, is clearly in contrast to the above multi-QD examples. This capability was a direct result of the concentric FRET relay, and all three of the possible FRET pathways ($FRET_1$, $FRET_2$, and $FRET_3$) were critical for multiplexed detection. Note that in nonconcentric relays that aim to transfer energy over longer radial distances from a QD, the $FRET_3$ pathway is typically too inefficient for this purpose.

Recently, we demonstrated a very different type of concentric FRET relay where energy was transferred from an LTC donor to a QD acceptor (FRET-I), which then served as a donor for A647 (FRET-II).[47,48] Multiplexed detection of two target oligonucleotides[47] and two target proteases[48] was possible using this assembly; however, the multiplexed information was encoded in "prompt" (QD→A647) and "time-gated" (LTC→QD→A647) temporal channels using the millisecond lifetime of the LTC. This format, however, required an instrument capable of collecting time-gated fluorescent spectra. Here, the QD→A555→A647 concentric FRET relay encodes multiplexed information entirely in spectral channels, negating the requirement of time-gating and offering compatibility with a much wider range of spectrofluorimeters, plate readers, and fluorescence microscopes commonly found in laboratories. As such, the current FRET relay is much more amenable to application with tissue culture or animal models, where it is anticipated to offer visualization and quantitative, ratiometric sensing of coupled proteolytic pathways without the challenge of having to target and deliver two different types of nanoparticle probe. Prospective future applications include tracking zymogen (pro-enzyme) activation, such as with the caspases during apoptosis,[49] or the action of multiple matrix metalloproteinases during cancer progression.[50]

In conclusion, we have demonstrated the assembly of a FRET relay comprising a central green-emitting QD scaffold and concentrically arranged A555 and A647 dyes using peptide bridges. Energy is preferentially transferred from the QD to the A555 ($FRET_1$) and then to the A647 ($FRET_2$), although direct energy transfer from the QD to the A647 ($FRET_3$) also occurs with lower efficiency. In conjunction with modeled predictions of energy transfer efficiency, we used the concentric FRET relay to show that peptides self-assembled to QDs *via* polyhistidine motifs have, to a first approximation, an equidistant distribution across the surface of a QD. We then demonstrated the simultaneous detection of the activity of two proteases using the concentric FRET relay, including the activation of a zymogen (pro-ChT) to an active protease (ChT) *via* the activity of an upstream protease (TRP). The concentric FRET relay should be applicable with a variety of colors of initial QD donor and various fluorescent dye acceptors, provided that the spectral overlap affords analogous $FRET_1$, $FRET_2$, and $FRET_3$ pathways. The concentric relay has strong potential for spectroscopic determination of both the radial dimensions and interfacial arrangements that characterize QD bioconjugates and for enabling "smarter" QD-FRET probes that offer multiplexed detection in a single vector.

MATERIALS AND METHODS

Quantum Dots, Dyes, and Buffer. CdSe/ZnS was synthesized and coated with poly(ethylene glycol)-appended dihydrolipoic acid (DHLA-PEG) ligands as described previously.[51,52] The structure of the ligand can be found in the Supporting Information (Scheme S1). The PEG provides colloidal stability across a wide range of pH and ionic strength. Alexa Fluor 555 C2 maleimide and Alexa Fluor 647 C2 maleimide were from Invitrogen by Life Technologies (Carlsbad, CA). All experiments were done in phosphate buffered saline (PBS; 10 mM, pH 7.4, 137 mM NaCl, 3 mM KCl).

Enzymes. Trypsin (from bovine pancreas; TPCK treated, essentially salt-free, lyophilized powder, ≥10 000 BAEE units/mg protein; enzyme commission number: 3.4.21.4), α-chymotrypsin (from bovine pancreas; TLCK treated, type VII, essentially salt-free, lyophilized powder, ≥40 units/mg protein; enzyme commission number: 3.4.21.1), and α-chymotrypsinogen A (from bovine pancreas; essentially salt-free, lyophilized powder; ≤1 unit/mg ChT prior to activation; ≥40 units/mg solid once activated) were from Sigma-Aldrich (St. Louis, MO).

Peptides and Labeling. Peptides were obtained from Biosynthesis, Inc. (Lewisville, TX) and were labeled in-house. Approximately 1 mg of peptide was dissolved in 20 μL of 50% v/v acetonitrile (aq), then diluted with 500 μL of PBS. The peptide solution was added to 1 mg of A647-maleimide (Invitrogen) dissolved in 10 μL of DMSO. Residual peptide was dissolved in 250 μL of PBS and also added to the A647-maleimide. The reaction was agitated at room temperature for 4–6 h and left at 4 °C overnight prior to purification. Peptides were purified over nickel(II)-nitrilotriacetic acid (Ni^{2+}-NTA) (Qiagen, Valencia, CA), desalted using a reverse-phase oligonucleotide purification cartridge (OPC; Applied Biosystems by Life Technologies,

Foster City, CA), and dried as described elsewhere.[25] Slight modifications to the published protocol are noted in the Supporting Information.

PL Measurements. PL emission spectra were measured using an Infinite M1000 fluorescence plate reader (Tecan, Research Triangle Park, NC). All samples were measured after aliquoting into a nonbinding 96-well microtiter plate. The excitation wavelength was 400 nm, which reduced direct excitation of the A555 and A647 to negligible levels. In calibration experiments, full PL spectra were measured for each well; in kinetic assays, PL was measured at 520, 570, and 670 nm for each well, in series, at 3 min intervals.

Calibration Samples. $[Sub_{ChT}(A555)]_M$-QD-$[Sub_{TRP}(A647)]_N$ conjugates were prepared in two steps. First, stock solutions were made by mixing 150 pmol of QD with 150*M* pmol of $Sub_{ChT}(A555)$, diluting with PBS to 500 μL, and incubating at room temperature for 1.5 h. Next, 15 pmol of the $[Sub_{ChT}(A555)]_M$-QD conjugates (in 50 μL of PBS) was mixed with 15*N* pmol (in 50 μL PBS) of $Sub_{TRP}(A647)$ and left to stand at room temperature for 2 h. The $Sub_{TRP}(A647)$ was taken from a stock solution with 150*N* pmol in 500 μL of PBS. This procedure was repeated for the ranges M = 0−7 and N = 0−7, yielding a total of 64 samples (8 × 8 matrix). PL spectra were then measured in the fluorescence plate reader.

Numerical Deconvolution of PL Contributions. The composite PL spectra for the QD, A555, and A647 emission were numerically deconvolved. The peak emission wavelength for the QD, λ_{QD} = 520 nm, was fully resolved from those for the A555 and A647. In contrast, the PL at the peak emission wavelengths for A555 and A647 ($\lambda_{A555} \approx 570$ nm and $\lambda_{A647} \approx 670$ nm) also had contributions from the QD and both QD + A555, respectively. The peak PL intensities for each emitter, I_X, were thus given by eqs 2−4, where ${}_X\sigma_\lambda$ is a correction factor for the PL contribution of emitter X at wavelength λ, as a percentage of its resolved peak PL intensity. These cross-talk correction factors were measured from PL spectra of each emitter individually. The values of the correction factors were ${}_{QD}\sigma_{570}$ = 0.019, ${}_{QD}\sigma_{670}$ = 0.016, and ${}_{A555}\sigma_{670}$ = 0.076.

$$I_{QD} = I_{520} \tag{2}$$

$$I_{A555} = I_{570} - {}_{QD}\sigma_{570} I_{QD} \tag{3}$$

$$I_{A647} = I_{670} - {}_{QD}\sigma_{670} I_{QD} - {}_{A555}\sigma_{670} I_{A555} \tag{4}$$

Calculation of PL Ratios. The PL intensity data were converted into dye/QD PL ratios, ρ_X, according to eqs 5 and 6, where α_X is a correction factor (the area-to-peak height ratio) for the PL spectrum of emitter X. The values of the correction factors were α_{QD} = 41.0, α_{A555} = 49.0, and α_{A647} = 49.1.

$$\rho_{A555} = \frac{\alpha_{A555} I_{A555}}{\alpha_{QD} I_{QD}} \tag{5}$$

$$\rho_{A647} = \frac{\alpha_{A647} I_{A647}}{\alpha_{QD} I_{QD}} \tag{6}$$

FRET Efficiencies. The calibration data were analyzed to extract FRET efficiencies using donor quenching efficiencies according to eq 7, where I_D is the unquenched donor PL intensity and I_{DA} is the PL intensity in the presence of acceptor. The $FRET_1$ and $FRET_3$ efficiencies as a function of the ensemble average conjugate valences, M (N = 0) and N (M = 0), respectively, were fit with eq 8 to account for the Poisson distribution of actual conjugate valences, m and n.[31] The r/R_0 term was the fitting parameter in a least-squares algorithm. Homogeneous FRET efficiencies, $E(m)$, for each conjugate valence were extracted in parallel.

$$E = 1 - (I_{DA}/I_D) \tag{7}$$

$$E(M) = \sum_{m=0}^{25} p(M,m)E(m) = \sum_{m=0}^{25} \frac{M^m e^{-M}}{m!} \frac{m}{m + (r/R_0)^6} \tag{8}$$

Spectral overlap integrals and Förster distances, R_0, were calculated as described in the Supporting Information.

Modeling $FRET_2$ Efficiency. The ensemble $FRET_2$ efficiency was calculated from quenching of the $FRET_1$-sensitized A555 PL (excitation at 400 nm), for each value of M across N = 0−7, using eq 7. The $FRET_2$ efficiency was modeled by treating the QD as a sphere (~5.6 nm diameter) with binding sites on its surface. The M A555 and N A647 dyes of a particular QD were positioned ~5 nm from the center of the sphere, on outward radial projections from the binding sites (*i.e.*, on the surface of a concentric sphere ~10 nm diameter). The specific locations of each dye were determined according to one of two models. In the "equidistant" model, the $M + N$ dye positions were evenly distributed over the surface of the 10 nm sphere (see Supporting Information) and only the identity of the dye at each position was chosen randomly. In the "random" model, 50 *candidate* dye positions (corresponding to the maximum peptide loading[33]) were evenly distributed over the surface of the 10 nm sphere, and the exact dye locations of each QD were selected at random from these candidate positions. Note that the random and equidistant models become equivalent when $M + N$ = 50. For each of the two models, an ensemble of QDs was created and included Poisson distributions for M and N to account for deviations from the average ensemble stoichiometry at the single particle level (see Supporting Information).

The overall FRET efficiencies were computed from ensemble averages of the efficiencies for the individual QD-$A555_m$-$A657_n$. An ensemble size of 2000 was sufficient for reliable statistics. The calculations of the individual efficiencies of the QDs were performed both without and with the inclusion of homo-FRET between the donors. When homo-FRET is not considered, the situation is simple because FRET only occurs between the particular excited donor and the various acceptors. The corresponding efficiency formula is given by eq 9, where R_0^{DA} is the Förster distance for the A555−A647 dye pair and d_{DA_j} is the distance between the excited donor and the jth acceptor. Since the conditions of the experiment were such that only one donor A555 was excited at any time, each A555 dye was treated as if it were isolated. QD configurations with multiple *potential* donors (M > 1) were considered as different members of the ensemble to be averaged over. Adjustments to the model to account for homo-FRET are given in the Supporting Information.

$$E_{DA} = \frac{\sum_{j=1}^{N} [R_0^{DA}/d_{DA_j}]^6}{1 + \sum_{j=1}^{N} [R_0^{DA}/d_{DA_j}]^6} \tag{9}$$

Enzyme Assays. Nominal $[Sub_{ChT}(A555)]_6$-QD-$[Sub_{TRP}(A647)]_6$ were prepared with *ca.* 375 pmol of QD, 2.2 nmol $Sub_{ChT}(A555)$, and 2.2 nmol $Sub_{TRP}(A647)$ in 825 μL of PBS. Initial PL measurements suggested that the final conjugates were closer to $[Sub_{ChT}(A555)]_5$-QD-$[Sub_{TRP}(A647)]_5$ as noted in the Results and Discussion. A series of TRP dilutions were prepared in PBS at 3× the final desired concentrations (0.42−27 nM) and 33 μL added to a series of wells in a microtiter plate. In assays with only TRP, 33 μL of PBS was also added to the wells. In assays with ChT or pro-ChT, 33 μL of the appropriate (pro-)enzyme solution (3× final concentration) was added to the wells for a concentration of either 40 nM ChT or 39 nM pro-ChT in the assays (solutions were prepared at fixed weight/volume; the small difference in molar concentration was due to the different molecular weights for ChT and pro-ChT). All assays were initiated by adding 33 μL (15 pmol) of QD conjugates with PL measurements starting immediately thereafter.

Conversion of PL Ratios to Numbers of Peptides. Each (M,N) combination of A555 and A647 per QD was mapped to a unique point on a plot of ρ_{A647} *versus* ρ_{A555}; see Figure 4C. While this result demonstrated that multiplexed detection was possible, it did not permit direct analysis since ρ_{A647} and ρ_{A555} were functions of both M and N. The calibration data in Figure 4 was used to fit two functions, eq 10 and eq 11, which are strictly empirical in form and in the value of the constant terms (see Supporting Information). Given the PL ratios measured from enzyme assays, (ρ_{A555}, ρ_{A647}), eqs 10 and 11 were used in an

iterative scheme to determine the corresponding (*M*,*N*) at each time point.

$$M = (a_1N + a_2)\rho_{A555}^2 + (a_3N + a_4)\rho_{A555} + a_5N + a_6 \quad (10)$$

$$N = \exp\left[\frac{-(\rho_{A647} - b_1M + b_2)}{b_3M + b_4}\right] + b_5M^3 + b_6M^2 + b_7M + b_8 \quad (11)$$

Conflict of Interest: The authors declare no competing financial interest.

Acknowledgment. The authors acknowledge financial support from NRL, NRL NSI, ONR, and DTRA-JSTO MIPR #B112582M. W.R.A. is grateful to NSERC for support through a postdoctoral fellowship.

Supporting Information Available: Structure of the DHLA-PEG ligand, quantum yield measurements, calculation of spectral overlap integrals, Förster distances, and relative energy transfer rates, details of the random model with different numbers of binding sites, details of homo-FRET modeling, variation of the two-step assembly method, time-dependent changes in PL signals during assays, calculation of specificity constants, activation assays with standard fluorogenic indicators. This material is available free of charge *via* the Internet at http://pubs.acs.org.

REFERENCES AND NOTES

1. Rosenthal, S. J.; Chang, J. C.; Kovtun, O.; McBride, J. R.; Tomlinson, I. D. Biocompatible Quantum Dots for Biological Applications. *Chem. Biol.* **2011**, *18*, 10–24.
2. Ho, Y. P.; Leong, K. W. Quantum Dot-Based Theranostics. *Nanoscale* **2010**, *2*, 60–68.
3. Algar, W. R.; Susumu, K.; Delehanty, J. B.; Medintz, I. L. Semiconductor Quantum Dots in Bioanalysis: Crossing the Valley of Death. *Anal. Chem.* **2011**, *83*, 8826–8837.
4. Hötzer, B.; Medintz, I. L.; Hildebrandt, N. Fluorescence in Nanobiotechnology: Sophisticated Fluorophores for Novel Applications. *Small* **2012**, *8*, 2297–2326.
5. Jin, Z.; Hildebrandt, N. Semiconductor Quantum Dots for *In Vitro* Diagnostics and Cellular Imaging. *Trends Biotechnol.* **2012**, *30*, 394–403.
6. Algar, W. R.; Tavares, A. J.; Krull, U. J. Beyond Labels: A Review of the Application of Quantum Dots as Integrated Components of Assays, Bioprobes, and Biosensors Utilizing Optical Transduction. *Anal. Chim. Acta* **2010**, *673*, 1–25.
7. Medintz, I. L.; Mattoussi, H. Quantum Dot-Based Resonance Energy Transfer and Its Growing Application in Biology. *Phys. Chem. Chem. Phys.* **2009**, *11*, 17–45.
8. Boeneman, K.; Prasuhn, D. E.; Blanco-Canosa, J. B.; Dawson, P. E.; Melinger, J. S.; Ancona, M.; Stewart, M. H.; Susumu, K.; Huston, A.; Medintz, I. L. Self-Assembled Quantum Dot-Sensitized Multivalent DNA Photonic Wires. *J. Am. Chem. Soc.* **2010**, *132*, 18177–18190.
9. Tikhomirov, G.; Hoogland, S.; Lee, P. E.; Fischer, A.; Sargent, E. H.; Kelley, S. O. DNA-Based Programming of Quantum Dot Valency, Self-Assembly and Luminescence. *Nat. Nanotechnol.* **2011**, *6*, 485–490.
10. Freeman, R.; Liu, X.; Willner, I. Chemiluminescent and Chemiluminescence Resonance Energy Transfer (CRET) Detection of DNA, Metal Ions, and Aptamer-Substrate Complexes Using Hemin/G-Quadruplexes and CdSe/ZnS Quantum Dots. *J. Am. Chem. Soc.* **2011**, *133*, 11597–11604.
11. Liu, X.; Freeman, R.; Golub, E.; Willner, I. Chemiluminescence and Chemiluminescence Resonance Energy Transfer (CRET) Aptamer Sensors Using Catalytical Hemin/G-Quadruplexes. *ACS Nano* **2011**, *5*, 7648–7655.
12. So, M. K.; Xu, C.; Loening, A. M.; Gambhir, S. S.; Rao, J. Self-Illuminating Quantum Dot Conjugates for *In Vivo* Imaging. *Nat. Biotechnol.* **2006**, *24*, 339–343.
13. Xia, Z.; Xing, Y.; So, M. K.; Koh, A. L.; Sinclair, R.; Rao, J. Multiplex Detection of Protease Activity with Quantum Dot Nanosensors Prepared by Intein-Mediated Specific Bioconjugation. *Anal. Chem.* **2008**, *80*, 8649–8655.
14. Charbonnière, L. J.; Hildebrandt, N. Lanthanide Complexes and Quantum Dots: A Bright Wedding for Resonance Energy Transfer. *Eur. J. Inorg. Chem.* **2008**, *2008*, 3241–3251.
15. Geißler, D.; Charbonnière, L. J.; Ziessel, R. F.; Butlin, N. G.; Löhmannsröben, H. G.; Hildebrandt, N. Quantum Dot Biosensors for Ultrasensitive Multiplexed Diagnostics. *Angew. Chem., Int. Ed.* **2010**, *49*, 1396–1401.
16. Dennis, A. M.; Rhee, W. J.; Sotto, D.; Dublin, S. N.; Bao, G. Quantum Dot-Fluorescent Protein FRET Probes for Sensing Intracellular pH. *ACS Nano* **2012**, *6*, 2917–2924.
17. Boeneman, K.; Mei, B. C.; Dennis, A. M.; Bao, G.; Deschamps, J. R.; Mattoussi, H.; Medintz, I. L. Sensing Caspase 3 Activity with Quantum Dot-Fluorescent Protein Assemblies. *J. Am. Chem. Soc.* **2009**, *131*, 3828–3829.
18. Medintz, I. L.; Clapp, A. R.; Mattoussi, H.; Goldman, E. R.; Fisher, B.; Mauro, J. M. Self-Assembled Nanoscale Biosensors Based on Quantum Dot FRET Donors. *Nat. Mater.* **2003**, *2*, 630–638.
19. Lu, H.; Schöps, O.; Woggon, U.; Niemeyer, C. M. Self-Assembled Donor Comprising Quantum Dots and Fluorscent Proteins for Long-Range Fluorescent Resonance Energy Transfer. *J. Am. Chem. Soc.* **2008**, *130*, 4815–4827.
20. Sapsford, K. E.; Pons, T.; Medintz, I. L.; Higashiya, S.; Brunel, F. M.; Dawson, P. E.; Mattoussi, H. Kinetics of Metal-Affinity Driven Self-Assembly between Proteins or Peptides and CdSe–ZnS Quantum Dots. *J. Phys. Chem. C* **2007**, *111*, 11528–11538.
21. Algar, W. R.; Prasuhn, D. E.; Stewart, M. H.; Jennings, T. L.; Blanco-Canosa, J. B.; Dawson, P. E.; Medintz, I. L. The Controlled Display of Biomolecules on Nanoparticles: A Challenge Suited to Bioorthogonal Chemistry. *Bioconjugate Chem.* **2011**, *22*, 825–858.
22. Shi, Z. S.; Olson, C. A.; Bell, A. J.; Kallenbach, R. N. Stabilization of α-Helix Structure by Polar Side-Chain Interactions: Complex Salt Bridges, Cation–π Interactions, and C–H···O H-Bonds. *Biopolymers* **2001**, *60*, 366–380.
23. Scheer, M.; Grote, A.; Chang, A.; Schomburg, I.; Munaretto, C.; Rother, M.; Söhngen, C.; Stelzer, M.; Thiele, J.; Schomburg, D. BRENDA, The Enzyme Information System in 2011. *Nucleic Acids Res.* **2011**, *39*, D670–D676.
24. Sweeny, P. J.; Walker, J. M., Proteolytic Enzymes for Peptide Production. In *Enzymes of Molecular Biology*; Burrell, M. M., Ed.; Humana Press: Totowa, NJ, 1993; Vol. 16, pp 277–303.
25. Sapsford, K. E.; Farrell, D.; Sun, S.; Rasooly, A.; Mattoussi, H.; Medintz, I. L. Monitoring of Enzymatic Proteolysis on a Electroluminescent-CCD Microchip Platform Using Quantum Dot-Peptide Substrates. *Sens. Actuators, B* **2009**, *139*, 13–21.
26. Sapsford, K. E.; Granek, J.; Deschamps, J. R.; Boeneman, K.; Blanco-Canosa, J. B.; Dawson, P. E.; Susumu, K.; Stewart, M. H.; Medintz, I. L. Monitoring Botulinum Neurotoxin A Activity with Peptide-Functionalized Quantum Dot Resonance Energy Transfer Sensors. *ACS Nano* **2011**, *5*, 2687–2699.
27. Bizzozero, S. A.; Baumann, W. K.; Dutler, H. Kinetic Investigation of the α-Chymotrpysin-Catalyzed Hydrolysis of Peptide Susbtrates. *Eur. J. Biochem.* **1982**, *122*, 251–258.
28. Coombs, G. S.; Rao, M. S.; Olson, A. J.; Dawson, P. E.; Madison, E. L. Revisiting Catalysis by Chymotrypsin Family Serine Proteases Using Peptide Substrates and Inhibitors with Unnatural Main Chains. *J. Biol. Chem.* **1999**, *274*, 24074–24079.
29. Medintz, I. L.; Clapp, A. R.; Brunel, F. M.; Tiefenbrunn, T.; Uyeda, H. T.; Chang, E. L.; Deschamps, J. R.; Dawson, P. E.; Mattoussi, H. Proteolytic Activity Monitored by Fluorescence Resonance Energy Transfer through Quantum-Dot-Peptide Conjugates. *Nat. Mater.* **2006**, *5*, 581–589.
30. Suzuki, M.; Husimi, Y.; Komatsu, Y.; Suzuki, K.; Douglas, K. T. Quantum Dot FRET Biosensors That Respond to pH, to Proteolytic or Nucleolytic Cleavage, to DNA Synthesis, or to a Multiplexing Combination. *J. Am. Chem. Soc.* **2008**, *130*, 5720–5725.

31. Pons, T.; Medintz, I. L.; Wang, X.; English, D. S.; Mattoussi, H. Solution-Phase Single Quantum Dot Fluorescence Resonance Energy Transfer. *J. Am. Chem. Soc.* **2006**, *128*, 15324–15331.
32. Algar, W. R.; Malonoski, A.; Deschamps, J. R.; Blanco-Canosa, J. B.; Susumu, K.; Stewart, M. H.; Johnson, B. J.; Dawson, P. E.; Medintz, I. L. Proteolytic Activity at Quantum Dot-Conjugates: Kinetic Analysis Reveals Enhanced Enzyme Activity and Localized Interfacial "Hopping". *Nano Lett.* **2012**, *12*, 3793–3802.
33. Prasuhn, D. E.; Deschamps, J. R.; Susumu, K.; Stewart, M. H.; Boeneman, K.; Blanco-Canosa, J. B.; Dawson, P. E.; Medintz, I. L. Polyvalent Display and Packing of Peptides and Proteins on Semiconductor Quantum Dots: Predicted *versus* Experimental Results. *Small* **2010**, *6*, 555–564.
34. Berlier, J. E.; Rothe, A.; Buller, G.; Bradford, J.; Gray, D. R.; Filanoski, B. J.; Telford, W. G.; Yue, S.; Liu, J.; Cheung, C. Y.; *et al.* Quantitative Comparison of Long-Wavelength Alexa Fluor Dyes to Cy Dyes: Fluorescence of the Dyes and Their Bioconjugates. *J. Histochem. Cytochem.* **2003**, *51*, 1699–1712.
35. Uete, T.; Asahara, M.; Tsuchikura, H. A Fluorometric Determination of Trypsin-like Amidase Activity and Activity of Trypsin Inhibitors in Serum. *Clin. Chem.* **1970**, *16*, 322–326.
36. Zimmerman, M.; Ashe, B.; Yurewicz, E. C.; Patel, G. Sensitive Assays for Trypsin, Elastase, and Chymotrypsin Using New Fluorogenic Substrates. *Anal. Biochem.* **1977**, *78*, 47–51.
37. Chen, N.; Zou, J.; Wang, S.; Ye, Y.; Huang, Y.; Gadda, G.; Yang, J. J. Designing Protease Sensors for Real-Time Imaging of Trypsin Activation in Pancreatic Cancer Cells. *Biochemistry* **2009**, *48*, 3519–3526.
38. Zheng, J. FRET and Its Biological Application as a Molecular Ruler. In *Biomedical Applications of Biophysics*; Jue, T., Ed.; Humana Press: Totowa, NJ, 2010; Vol. 3, pp 119–136.
39. Morgner, F.; Geißler, D.; Stufler, S.; Butlin, N. G.; Löhmannsröben, H. G.; Hildebrandt, N. A Quantum-Dot-Based Molecular Ruler for Multiplexed Optical Analysis. *Angew. Chem., Int. Ed.* **2010**, *49*, 7570–7574.
40. Medintz, I. L.; Konnert, J. H.; Clapp, A. R.; Stanish, I.; Twigg, M. E.; Mattoussi, H.; Mauro, J. M.; Deschamps, J. R. A Fluorescence Resonance Energy Transfer-Derived Structure of a Quantum Dot-Protein Bioconjugate Nanoassembly. *Proc. Natl. Acad. Sci. U.S.A.* **2004**, *101*, 9612–9617.
41. Algar, W. R.; Krull, U. J. Adsorption and Hybridization of Oligonucleotides on Mercaptoacetic Acid-Capped CdSe/ZnS Quantum Dots and Quantum Dot-Oligonucleotide Conjugates. *Langmuir* **2006**, *22*, 11346–11352.
42. Boeneman, K.; Deschamps, J. R.; Buckhout-White, S.; Prasuhn, D. E.; Blanco-Canosa, J. B.; Dawson, P. E.; Stewart, M. H.; Susumu, K.; Goldman, E. R.; Ancona, M.; *et al.* Quantum Dot DNA Bioconjugates: Attachment Chemistry Strongly Influences the Resulting Composite Architecture. *ACS Nano* **2010**, *4*, 7253–7266.
43. Hohng, S.; Ha, T. Single-Molecule Quantum-Dot Fluorescence Resonance Energy Transfer. *Chem. Phys. Chem.* **2005**, *6*, 956–960.
44. Algar, W. R.; Krull, U. J. Toward a Multiplexed Solid-Phase Nucleic Acid Hybridization Assay Using Quantum Dots as Donors in Fluorescence Resonance Energy Transfer. *Anal. Chem.* **2009**, *81*, 4113–4210.
45. Lowe, S. B.; Dick, J. A. G.; Cohen, B. E.; Stevens, M. M. Multiplex Sensing of Protease and Kitnase Enzyme Activity *via* Orthogonal Coupling of Quantum Dot Peptide Conjugates. *ACS Nano* **2012**, *6*, 851–857.
46. Liu, J.; Lee, J. H.; Lu, Y. Quantum Dot Encoding of Aptamer-Linked Nanostructures for One-Pot Simultaneous Detection of Multiple Analytes. *Anal. Chem.* **2007**, *79*, 4120–4125.
47. Algar, W. R.; Wegner, D.; Huston, A. L.; Blanco-Canosa, J. B.; Stewart, M. H.; Armstrong, A.; Dawson, P. E.; Hildebrandt, N.; Medintz, I. L. Quantum Dots as Simultaneous Acceptors and Donors in Time-Gated Forster Resonance Energy Transfer Relays: Characterization and Biosensing. *J. Am. Chem. Soc.* **2012**, *134*, 1876–1891.
48. Algar, W. R.; Malanoski, A. P.; Susumu, K.; Stewart, M. H.; Hildebrandt, N.; Medintz, I. L. Multiplexed Tracking of Protease Activity Using a Single Color of Quantum Dot Vector and a Time-Gated Förster Resonance Energy Transfer Relay. *Anal. Chem.* **2012**, *84*, 10136–10146.
49. Riedl, S. J.; Shi, Y. Molecular Mechanisms of Caspase Regulation during Apoptosis. *Nat. Rev. Mol. Cell Biol.* **2004**, *5*, 897–907.
50. Folgueras, A. R.; Pendás, A. M.; Sánchez, L. M.; López-Otín, C. Matrix Metalloproteinases in Cancer: From New Functions to Improved Inhibition Strategies. *Int. J. Dev. Biol.* **2004**, *48*, 411–424.
51. Mei, B. C.; Susumu, K.; Medintz, I. L.; Mattoussi, H. Polyethylene Glycol-Based Bidentate Ligands To Enhance Quantum Dot and Gold Nanoparticle Stability in Biological Media. *Nat. Protoc.* **2009**, *4*, 412–423.
52. Mei, B. C.; Susumu, K.; Medintz, I. L.; Delehanty, J. B.; Mountziaris, T. J.; Mattoussi, H. Modular Poly(ethylene glycol) Ligands for Biocompatible Semiconductor and Gold Nanocrystals with Extended pH and Ionic Stability. *J. Mater. Chem.* **2008**, *18*, 4949–4958.